Seismic Analysis of Spatio-Temporal Fracture Generation at The Geysers EGS Demonstration Project

Douglas S. Dreger[1], O. Sierra Boyd[1], Roland Gritto[2], and Taka'aki Taira[1]

[1]Berkeley Seismological Laboratory, Berkeley, CA, 94720

[2]Array Information Technology, 2020 Cedar Street, Berkeley, CA 94709

Roland.Gritto@arrayinfotech.com

Keywords: EGS development, fracture characterization, moment tensor analysis, stress and fluid state and temporal changes

ABSTRACT

We analyzed seismicity near the EGS development at The Geysers, CA Prati-32 injection well to evaluate the development and the physical attributes of a subsurface fracture network. The goals of our study include the ability to estimate the orientation and the activated fracture area, to estimate stress orientation and stress orientation changes as well as fluid saturation and spatio-temporal changes in fluid saturation. We compiled a 168-event waveform-based seismic moment tensor catalog for events $0.7 \leq M_w \leq 3.9$ based on a semi-automated moment tensor analysis technique to be used for in-situ stress estimation during the injection phases. We found an approximate 15-degree counterclockwise rotation of the least compressive stress σ_3, and a rotation of the maximum compressive stress σ_1 toward the vertical as the injected volume of water increased. We developed a rupture-area magnitude scaling relationship of The Geysers earthquakes obtained from finite-source inversion for fault slip that reveals a very high correlation to published results. Based on the rupture area-magnitude relationship we mapped M_w from the LBNL earthquake catalog to estimate the activated fracture area and its location within the injection volume of Prati-32. Analysis of the Vp/Vs-ratio based on the double-difference Wadati technique revealed the development of an injection-derived steam plume during the early injection phase, particularly in the northern parts of the Prati-32 study area.

1. INTRODUCTION

Identifying, creating, and managing fractures and flow paths are essential tasks during EGS resource development. The successful generation of a fracture network requires a priori knowledge of in-situ stress and natural fracture orientation and spacing, among others. However, because the orientation and magnitude of in-situ stress may not be reliably available and injecting fluids at high rates and volume may disturb the natural stress state, it is advantageous to monitor in-situ stress during the injection process. Knowing the stress evolution, the size of the fractures and the nature of the rupture process, as well as the spatial distribution of the fluid flow are essential to control the generation of the fracture network.

Our research goal is to improve technology to assess in-situ stress magnitude and orientation, kinematic fracture parameters, rupture size, as well as temporal and volumetric distribution of the injected fluid during Enhanced Geothermal System (EGS) resource development. We leverage high-frequency seismic data recorded by the LBNL 34-station permanent geophone network and seismic broadband data recorded by a temporary 33-station seismometer network that operated in The Geysers during the injection phase of the Department of Energy Geothermal Technologies Office (DOE GTO) funded EGS demonstration project at Prati-32.

We have developed technology to (1) estimate in situ stress and temporal stress changes based on a semi-automatically derived moment tensor catalog, to (2) estimate a scaling relationship for small magnitude events to appraise the activated rupture area and fracture volume and to (3) estimate fluid saturation and spatio-temporal changes throughout the injection phase at Prati-32. In the following, we present our results obtained for the EGS demonstration project at Prati-32.

2. SEISMIC MOMENT TENSORS AND STRESS INVERSION

2.1 The Geysers EGD Demonstration Project

The Geysers geothermal reservoir in northern California is the largest geothermal reservoir in the world with approximately 1.6 GW installed electric capacity and current production of about 750 MW. The region around Prati-32 in the northwest Geysers is presented in Figure 1, which shows our study area, the location of the Prati-32 injection well, nearby seismic stations, and known faults.
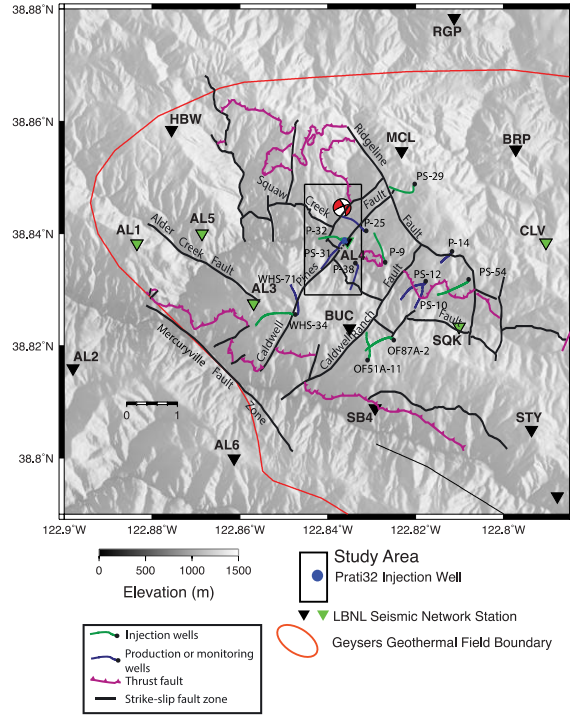
Figure 1: Map showing study area (1x2 km rectangle), Prati-32 well, LBNL seismic stations, and faults.

2.1 Seismic Moment Tensor and Stress Inversion

We have developed a semi-automated moment tensor analysis technique to construct a catalog of 166 moment tensor solutions of $0.7 \leq M \leq 3.9$ events that occurred within the study area during injection. The timeline of these solutions that were obtained from three-component waveform inversion (Gritto et al., 2016; Minson and Dreger, 2008; Pasyanos et al., 1996) is presented in Figure 2 superimposed on the Prati-32 fluid injection rate. Following the start of injection, an increase in both, frequency and magnitude of events is apparent, with a decrease visible during the injection hiatus in 2012. The largest events appear correlated with changes in injection rate.
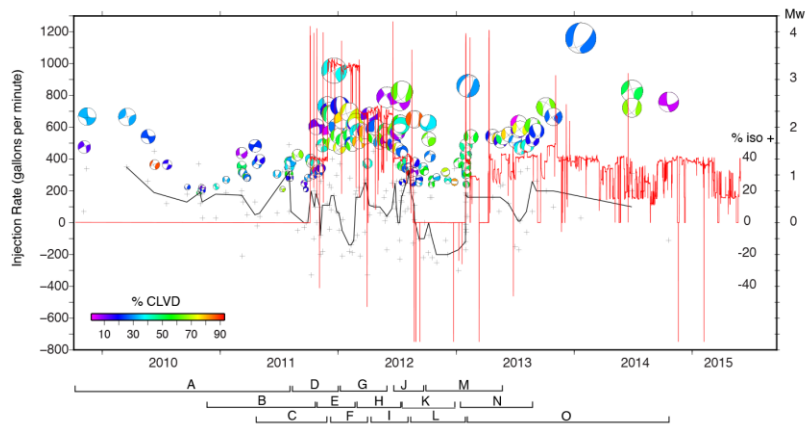

Figure 2: Seismic moment tensor solutions plotted with the 30-day Prati-32 injection rate.

The solutions of the moment tensor catalog were used to invert for the in-situ state of stress within the study region utilizing both the MSATSI software developed by Martinez-Garzon et al. (2014), which is based on the method of Hardebeck and Michael (2004, 2006), and the STRESSINVERSE software package developed by Vavrycuk (2014). We applied a sliding window containing 30 events for each time period of the stress inversion in which there was a 10-event overlap between time windows. Because it is not known which of the two possible nodal planes is the actual earthquake rupture plane, a random sampling of the nodal planes is bootstrapped to assess the

uncertainty in the estimated stress tensors in the MSATSI approach, while the STRESSINVERSE code uses an iterative method to find the nodal planes most consistent with the stress field given fault frictional properties.

The results show an interesting change in the orientation of the principal stress axes during injection operations. Stereonet plots of the orientation of principal stress axes σ_1 (red), σ_2 (green), and σ_3 (blue) for each time window are shown in the odd rows in Figures 1 A-O. The colored regions show the 95 percent confidence region from the bootstrap analysis. Initially there is an east-southeast orientation of the minimum compressive stress σ_3 (blue) and south-southwest maximum compressive stress σ_1 (red) in a predominantly strike-slip faulting environment.
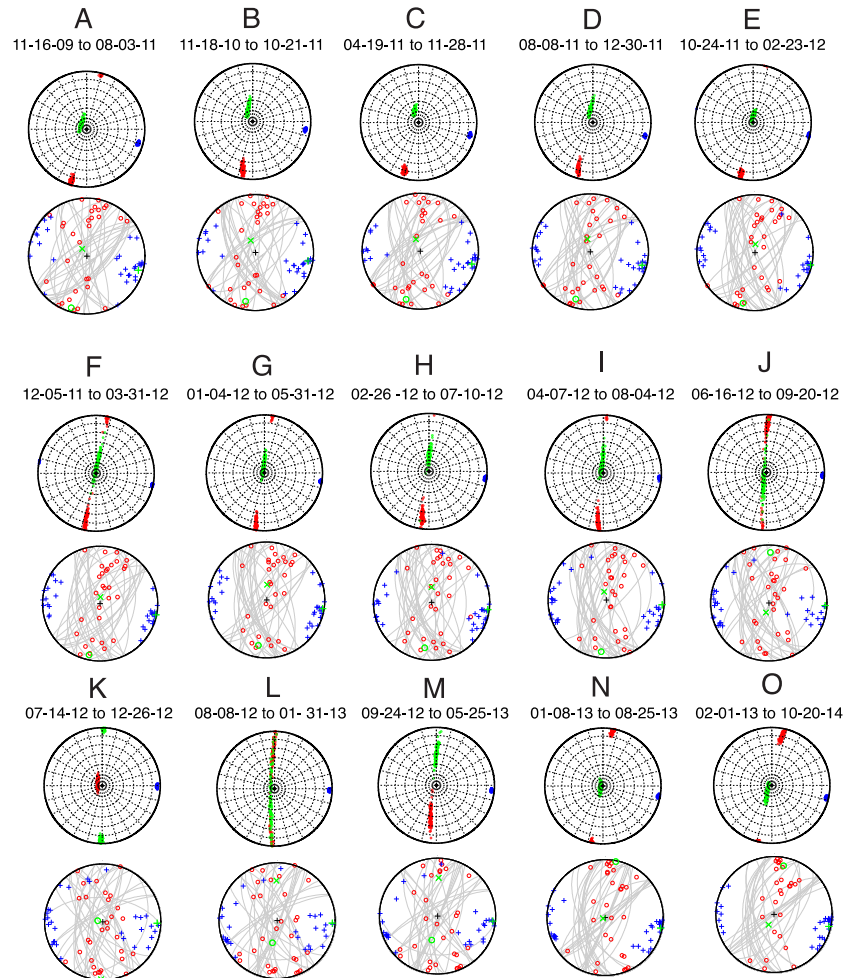

Figure 3: *Odd rows:* **Stereonet plots of principal stress orientations obtained using STRESSINVERSE (Vavrycuk, 2014) during 15 overlapping time periods labeled A - O. There are 30 focal mechanisms for each time period, except for the last time window with 28 focal mechanisms, with 66% overlap. The orientations of the maximum compressive stress σ_1 (red), intermediate stress σ_2 (green), and minimum compressive stress σ_3 (blue) are well constrained. The colored regions represent the 95% confidence intervals from the bootstrap analysis. Within each 95 percent confidence region, the best orientation of the principal stress axis is marked with a circle for σ_1, a cross for σ_2, and a plus symbol for σ_3.** *Even rows:* **Plots of principal stress orientation (green symbols) and pressure (red circles) and tension (blue crosses) axes of input focal mechanisms. Output nodal planes (gray lines) oriented for failure show greater variability when injection stops in windows K and L.**

Gradually with time during injection there is an approximately 15-degree counter-clockwise rotation of σ_3 until time window J ending September 20, 2012. This is followed by a marked rotation of σ_1 toward a more vertical orientation (time window K beginning in July 2012). This time window from July 14, 2012 - December 26, 2012 corresponds to a period when injection operations temporarily cease at Prati-32 from August 20, 2012 for a period of approximately 160 days until January 29, 2013. Subsequent time windows L (August 8, 2012 - January 31, 2013) and M (September 24, 2012 - May 25, 2013) also show a similar rotation in orientation that corresponds to further changes in injection operations. Prati-32 injection resumes in early February 2013 until March 12, 2013. Prati State 31 continues to produce steam from December 5, 2012 until the well is shut-in mid-February 2013 due to a leak caused by corroded well casing.

In mid-February 2013 injection shifts to Prati State 31 at a rate of 300 gpm resulting in a migration of seismicity to the south in the vicinity of Prati State 31. Injection continues in Prati State 31 until March 21, 2013 when the well is repaired. Injection in Prati-32

Dreger et al.

resumes April 9, 2013. During this period the magnitude of σ_1 and σ_2 also begin to equalize indicating that the system is evolving to a more tensile environment in which the mechanisms are comprised of both strike-slip and normal types. The orientations of the principal stress axes return to a more initial strike-slip stress state during time window N beginning January 8, 2013 and continue through time window O ending October 20, 2014.

Figure 3 even rows show plots of principal stress orientation (green symbols) and pressure (red circles) and tension (blue crosses) axes of input focal mechanisms. Output nodal planes (gray lines) oriented for failure show predominantly NW-SE and NE-SW orientations with greater variability including E-NE orientations when injection stops in windows K and L.

3. FINITE SOURCE RUPTURE ESTIMATION

3.1 Seismic Moment Rate Function

For finite-source investigation it is necessary to find highly correlated pairs of events to determine the seismic moment rate function at a recording station using the method of waveform deconvolution of a small magnitude earthquake. Usually events need to be close in space on the order of 200 m and have similar faulting mechanisms to achieve sufficient correlation. Furthermore, a difference of at least one order magnitude is required to minimize the source contribution in the resulting waveform. The smaller-magnitude empirical Green's function (eGf) event is spectrally deconvolved from the larger-magnitude target event. The resulting spectrum is then inverse Fourier transformed yielding a pulse that is interpreted as the far-field source-time function (Mori, 1993). The principle of the seismic moment rate function is presented using the example of a Mw 2.47 event on August 25, 2013. Date, time, latitude, longitude, depth, and catalog magnitude of the target and selected eGf event are shown in Table 1.

Table 1: Catalog, date, time, latitude, longitude, depth and magnitude from DOE EGS LBNL catalog for selected target and eGf events.

	Catalog	Date	Time	Latitude	Longitude	Depth	Magnitude
Target	LBNL	2013/08/25	14:06:47.39	38.84297	-122.83650	2.10	Mw 2.47
eGf	LBNL	2013/09/14	11:40:40.15	38.84298	-122.83900	2.135	Mw 1.13

We investigated the moment tensor of the target event using data filtered in passband 0.7 – 1.7 Hz. Waveform data were downloaded from the NCEDC for stations in the LBNL Berkeley Geysers (BG) seismic network. We used event times and locations as specified in the DOE EGS LBNL catalog. To constrain the moment tensor we used the source-type inversion methodology of Nayak and Dreger (2015) to explore the source-type-specific space of combined first-motion and waveform data. The combined first-motion and waveform data full moment tensor inversion results in a decomposition of 41% double-couple (DC), 37% CLVD, and 22% ISO components, as presented in Figure 4, with a variance reduction (VR) of 63%. The interpretation for this oblique normal event is that its full moment tensor mechanism is composed of roughly equal parts DC-CLVD with a small negative volumetric component as shown in Table 2.
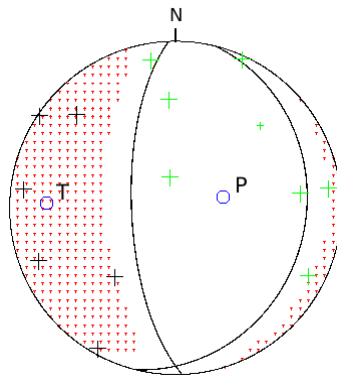

Figure 4: The constrained moment tensor solution uses first-motion polarity data plotted with plus symbols, up first motions (black), down first motions (green). The negative isotropic component evidenced by the lack of shading in the compressive quadrants indicates an implosive mechanism.

Table 2: Target event combined waveform and first motion full moment tensor parameters. Strike, rake and dip for both nodal planes.

Bowers Moment (dyne-cm)	Mw	Strike	Rake	Dip	%DC	%CLVD	%ISO
1.7E+19	2.09	14/178	-75/-96	22/68	41	37	22

4

The empirical Green's function approach assumes that the target and eGf pair are co-located events having a similar source mechanism with a difference in magnitude of at least one unit. Suitable eGf events horizontally located within 200 m from larger target events were found in the DOE EGS LBNL catalog. The eGf waveforms were then deconvolved from the target waveforms to identify those that produced pulse-like moment rate functions (MRF) with the highest signal to noise ratio. The pulse widths of the resulting MRFs range from 0.1075 s at station HBW in the north to a narrow width of 0.046 s at station SB4 in the south, suggestive of a north to south rupture. The MRFs for the target event are presented in Figure 5.
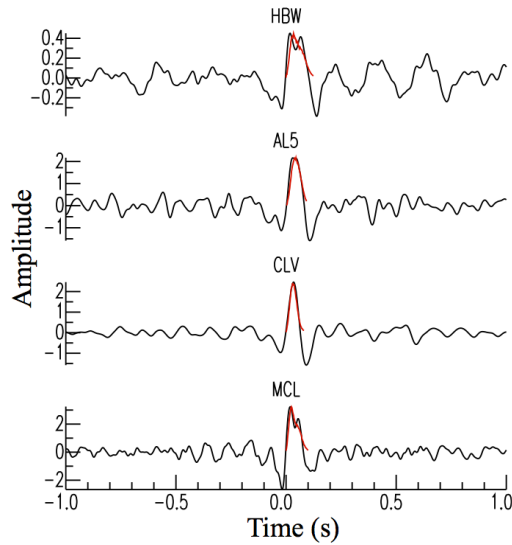

Figure 5: Stacked MRF pulse trains (black), cut pulses (red) for stations (a) HBW (b) AL5 (c) CLV and (d) MCL.

3.2 Finite-Source Analysis

In the following, we summarize how finite-source parameters are obtained from MRFs, such as the ones shown in the last section. The method used to invert the MRF for slip distribution is based on the methods of Mori and Hartzell (1990), Mori (1993), Dreger (1997), and Dreger et al. (2007). Before inverting for finite-source dimensions the MRFs are normalized such that their area is equal to the scalar seismic moment of the target event. In this study we used a 61 x 61 gridded fault with dimensions of 1 km^2 with a corresponding subfault size of 16.4 m^2, and the DOE EGS LBNL catalog location and depth. The model assumes a constant rupture velocity of 0.8 times the shear wave speed at the source depth. The slip at each patch on the fault occurs with a slip velocity that is determined by the rise time of a 0.02 s fixed-width boxcar. The total allowable slip duration is 1 s. The subfault dimension is consistent with the 11.8 m wavelength for S waves with Vs = 2.94 km/s at 2.1 km depth and 250 Hz bandwidth. The inversion uses a slip positivity constraint and a smoothing constraint to minimize the spatial derivative of the slip. The smoothing weight is investigated by searching for the smallest value that produces a smoothed model with a fit close to the maximum fit to the data as measured by the variance reduction. The rupture area is determined by the number of subfaults with slip greater than 10% of the maximum slip and varies with smoothing parameter. This threshold is used to ignore small amplitude patches of slip that are poorly constrained by the inversion. Smoothing parameters of 2, 20, 200, and 2000 were investigated for an area ranging from 0.01 – 0.08 km^2, Table 3. The goodness of fit between the observed and synthetic MRFs is comparable for the strike, rake, and dip of both nodal planes yet one nodal plane with strike = 14, dip = 22, and rake = -75 has a smoothed and somewhat simpler slip distribution. The slip and stress change maps from the inversion of moment rate functions at four nearby stations for rupture velocity 80% of the local shear wave velocity are shown in the left and right columns, respectively, in Figures 6 (a-d). The distributions vary depending on the smoothing parameter 2, 20, 200, and 2000. For this event the peak stress drop is somewhat low < 5 MPa. Based on this modeling, the preferred model has a smoothing of 200 (Figure 6c).

Table 3: Finite-source model smoothing parameter, slip area, and goodness of fit.

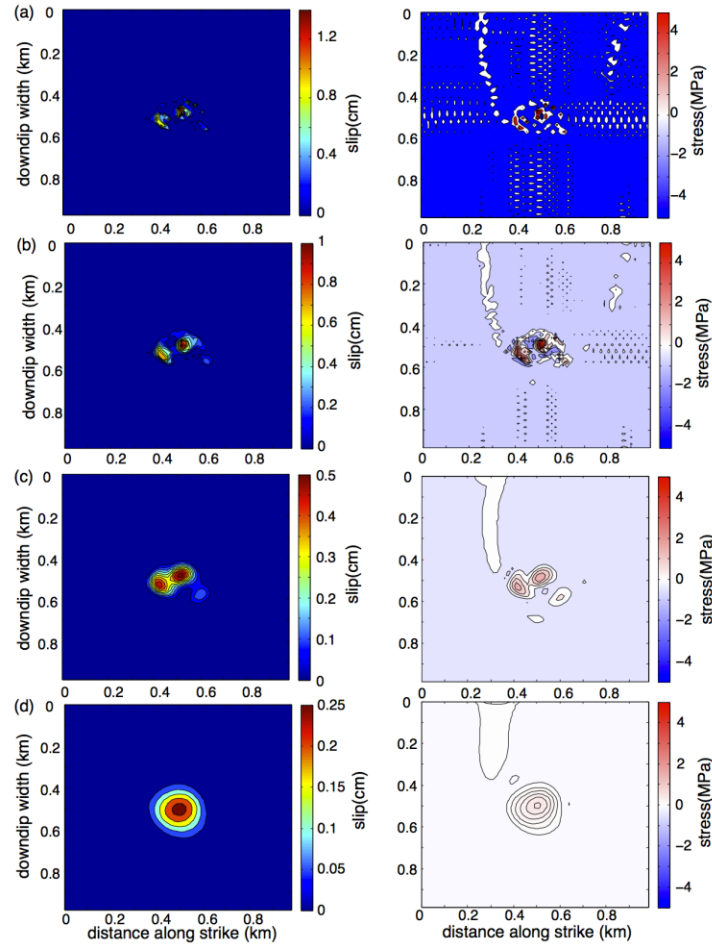| Smoothing	Slip Area (km^2)	Goodness of Fit %
2	0.0145	99.4
20	0.0223	99.3
200	0.0352	99.0
2000	0.0761	95.6

Figure 6: Slip (left column) and stress (right column) distributions from inversion of moment rate functions with smoothing parameters (a) 2 (b) 20 (c) 200 and (d) 2000. Stress change on the fault surface with red as stress drop and blue as stress increase.

3.3 Magnitude-Scaling Relationship

We have obtained finite-source models for nine earthquakes at The Geysers spanning the magnitude range from Mw 2.1 to 5.1. As shown in Figure 7, the estimated area for these events is consistent with the scaling laws of both Wells and Coppersmith (1994) and Leonard (2010). This is remarkable as those relationships were developed for events with Mw larger than 5.5, and the great majority of events in those studies are for earthquakes larger than Mw 6.0. The results in Figure 7 demonstrate that The Geysers earthquakes follow the self-similar scaling law, but may be on average slightly more compact, or exhibit higher stress drop (plot below the solid lines) than the average of the events in Wells and Coppersmith (1994) and Leonard (2010). The Geysers events are found to lie within the two-sigma curves for the Leonard (2010) relationship (gray dashed lines), which represent approximately 10 (upper dashed line) and 100 bar (lower dashed line) stress drops.
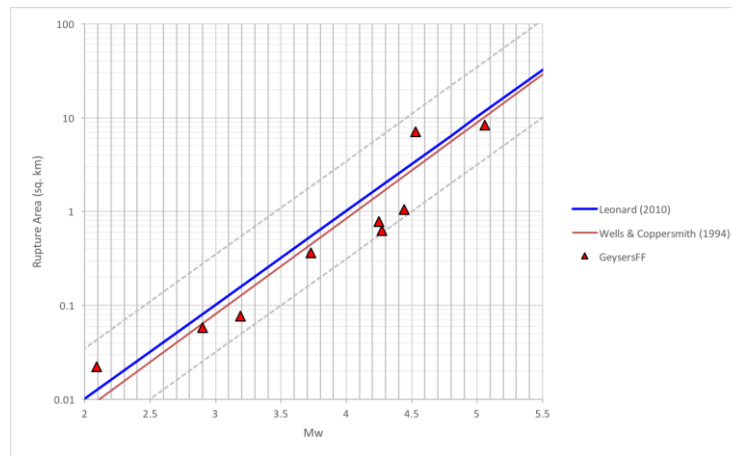
Figure 7: The Leonard (2010) (blue) and Wells and Coppersmith (1994) (orange) rupture area vs. Mw scaling laws are compared to area estimates for Geysers earthquakes obtained from finite-source inversion. The gray lines show the two-sigma errors for the Leonard (2010) relationship and represent approximately 10 bar (upper) and 100 bar (lower) stress drops.

The moment magnitude Mw estimates from the catalog derived for seismicity in the study area around Prati-32 were compared with those reported by LBNL, which are computed assuming a simplified spectral level method, and which are made available on the Northern California Earthquake Data Center (NCEDC) website. It was found that the LBNL Mw magnitudes from the NCEDC-hosted catalog are approximately 0.6 magnitude units larger, which are due to assumptions in the spectral estimation method. Applying a correction of the catalog magnitudes based on the waveform inversion constraint will enable using the LBNL catalog Mw for thousands of earthquakes that otherwise cannot be analyzed with the more computationally intensive approach presented above, as well as for events below the magnitude limit for moment tensor analysis in order to map the coseismic fracture density in the study area. Figure 8 shows a comparison of waveform Mw magnitudes from moment tensor analyses with the corrected LBNL spectral Mw magnitudes indicating that the correlation is very good.
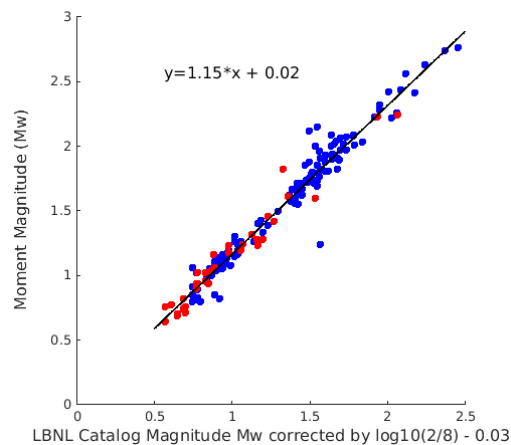

Figure 8: Comparison of waveform moment tensor Mw with LBNL catalog Mw. The LBNL Mw have been corrected by a factor of log10(2/8)-0.03 where the 2/8 ratio accounts for the difference between a theoretical half-space Green function and the semi-empirical half-space model. The -0.03 factor accounts for differences between the specific moment magnitude relationships used. Following correction, a regression of the Mw data recovers a nearly 1:1 slope and a zero intercept.

3.4 3D Fracture Network

Previously, we applied the Mw correction derived between our waveform results and those reported in the LBNL catalog to 7,416 events in the LBNL catalog spanning the period from November 16, 2009 through October 20, 2014, and subsequently applied the Leonard (2010) scaling law to convert to rupture area (Dreger et al., 2017). In the current paper, we selected 752 events from October 1, 2009 to September 30, 2015 with high accuracy locations from the LBNL catalog (Mw 0.3 -2.2), to construct a 3D representation of the fracture network below Prati-31 and Prati-32, for a representative image of the discrete fracture network stimulated by the injection of fluid into the hot rock. The high accuracy locations of the 752 events were determined based on a minimum of 16 travel times phase picks and a maximum RMS error between calculated and observed travel times of 0.05s. The rupture area associated with these events

where again estimated using the moment magnitudes and the Leonard (2010) scaling relationship. For a more realistic representation of the fracture network, we characterize the discreate fractures by circles with size, strike and dip orientation according to our magnitude scaling and stress inversion results. The diameter of the fracture circles was determined by the rupture area-scaling relationship, while the strike and dip were determined using statistics with a Gaussian distribution based on the results of the stress inversions, which indicated a σ_1 direction N20ºE with an uncertainty of 10º (two-sigma) and a dip of 80º with the same uncertainty. The result of the statistical representation of such a fracture network are presented in Figures 9-11. In these figures the rupture area is represented by the size of the circles, while the colored dots at the hypocenters denote the moment magnitude of the events. The shape of the circles has degenerated to ellipses, because of the compressed vertical axis (1:2) and the oblique view of the plot. The plots reveal that the highest concentration of fractures is located approximately 300 m to the north and 400 m below the bottom of the injection and production wells.
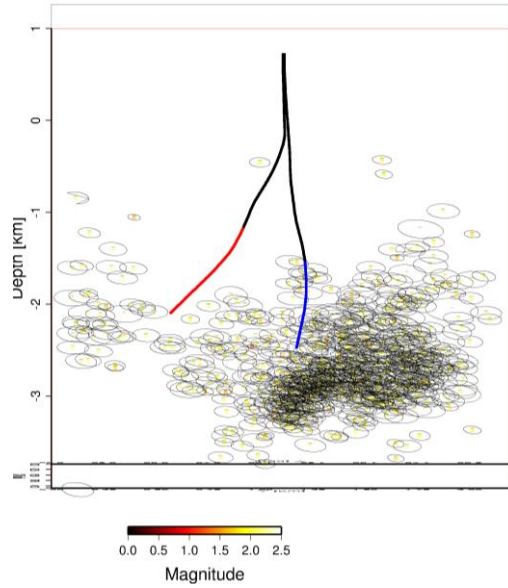

Figure 9: Statistical representation of the generated fracture network below production well Prati-31 (red) and injection well Prati-32 (blue). The circle diameters represent the rupture area, which the colored dots at the hypocenters denotes the moment magnitude. The shape of the circles is deformed to ellipses because the vertical axis is vertically compressed (1:2) and because of the fracture dip. View from east to west.
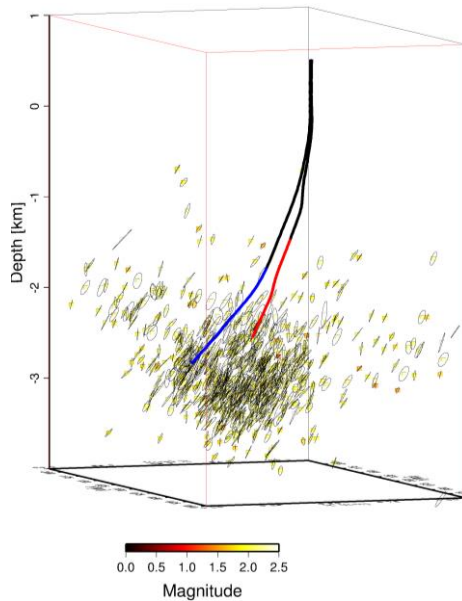

Figure 10: Same as Figure 9. View from southwest to northeast in the direction of σ_1.
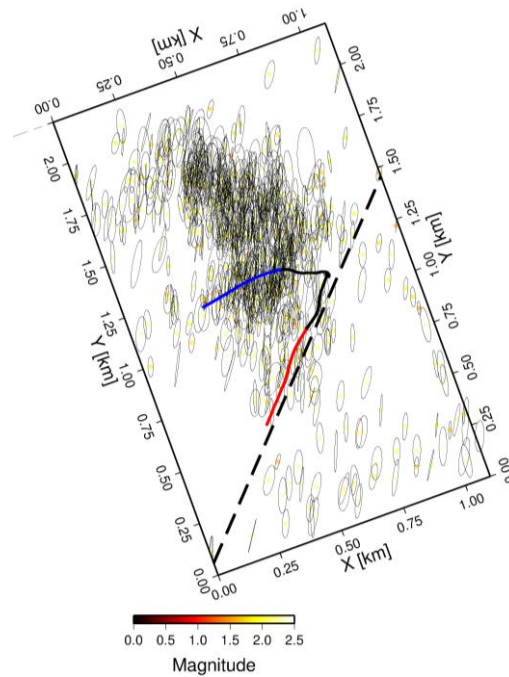
Figure 11: Same as Figure 9. View vertically down. The dashed black line approximates the trajectory of the Caldwell Pines Fault.

4. ESTIMATION OF SPATIO-TEMPORAL FLUID SATURATION

The double-difference Wadati (DDW) technique has been applied to estimate temporal changes of fluid distribution in fault zones (Lin and Shearer, 2007, 2009), in volcanic regions (Dahm and Fischer, 2013) and recently engineered geo-reservoirs (Gritto et al., 2016). The application of the DDW technique is based on estimating the ratio of P- and S-wave velocity (Vp/Vs) in the subsurface. Vp/Vs has been used in seismological applications and seismic exploration to probe the subsurface for liquid and gaseous fluids. Applications in the oil and gas industry include analysis of Vp/Vs to trace fluids in reservoirs during second and tertiary oil recovery (Gritto et al., 2004a) as well as during fracking campaigns. Seismological investigations include tracing the movement of fluids during volcanic unrest (Dahm and Fischer, 2013, Lin, 2013) and to image fluids in fault zones (Lin and Shearer, 2007, 2009). In general, high Vp/Vs indicates the presence of liquid fluids in the subsurface (Moos and Zoback, 1983, Gritto et al., 2004b, Gritto and Jarpe, 2014), while low Vp/Vs indicates the presence of gaseous fluids (Julian et al., 1996).

In the study by Gritto et al. (2016), DDW was applied to high-accuracy P- and S-wave differential travel times derived from waveform cross correlation to image fluid saturation in the injection volume of the Prati-32 study area based on Vp/Vs-ratio. Estimating Vp/Vs-ratio from DDW requires accurate fitting techniques, since the differential travel times of the seismic waves propagating from neighboring events to a common recording station can be quite small. At the same time, differential travel time data are contaminated by errors in both P- and S-wave times including outliers in some of the data. In cases like these, common fitting techniques such as linear least squares or median fitting are inadequate to accurately estimate the fit to the data, even when errors in both variables are considered (Gritto et al., 2016). Therefore, a robust fitting technique based on the L1-L2 norm was implemented to estimate Vp/Vs-ratio from differential P- and S-wave travel times of earthquake clusters on a Wadati diagram.

In their initial analysis, Gritto et al (2016) investigated temporal changes in fluid saturation comparing pre- to post-injection seismicity in the study area of Prati-32. They reported a pre-injection Vp/Vs ratio of 1.76 with a standard deviation of 0.04. The value, being close to the typical Vp/Vs of 1.73 for crustal rocks, was interpreted to indicate that the reservoir rocks in the study area are undisturbed due to the absence of injection and production activities. Their post-injection analysis revealed a post-injection drop in Vp/Vs to 1.67 with a standard deviation of 0.04. This statistically significant drop in Vp/Vs was interpreted by the development of a steam plume in the injection volume of Prati-32, due water flashing to steam in this high-temperature region of the reservoir.

In the current paper, we analyzed the spatial variation of the fluid saturation in the injection volume below Prati-32. It was shown in Figure 9, that the generated fractures in the study area are not homogeneously distributed. It was seen that the highest concentration of fractures developed in the northern part of the region, whereas the southern region exhibited a lower fracture concentration. Therefore, it was investigated, whether the fluid saturation is spatially correlated to fracture density. Figure 12a shows a map view with the distribution of earthquakes with high accuracy locations recorded during the first three months of injection. The analysis of these events led to the post-injection Vp/Vs ratio of 1.67 ± 0.04, as reported by Gritto et al. (2016). This sequence was subsequently divided into a northern and a southern region, which are shown in Figure 12b and 12c, respectively.
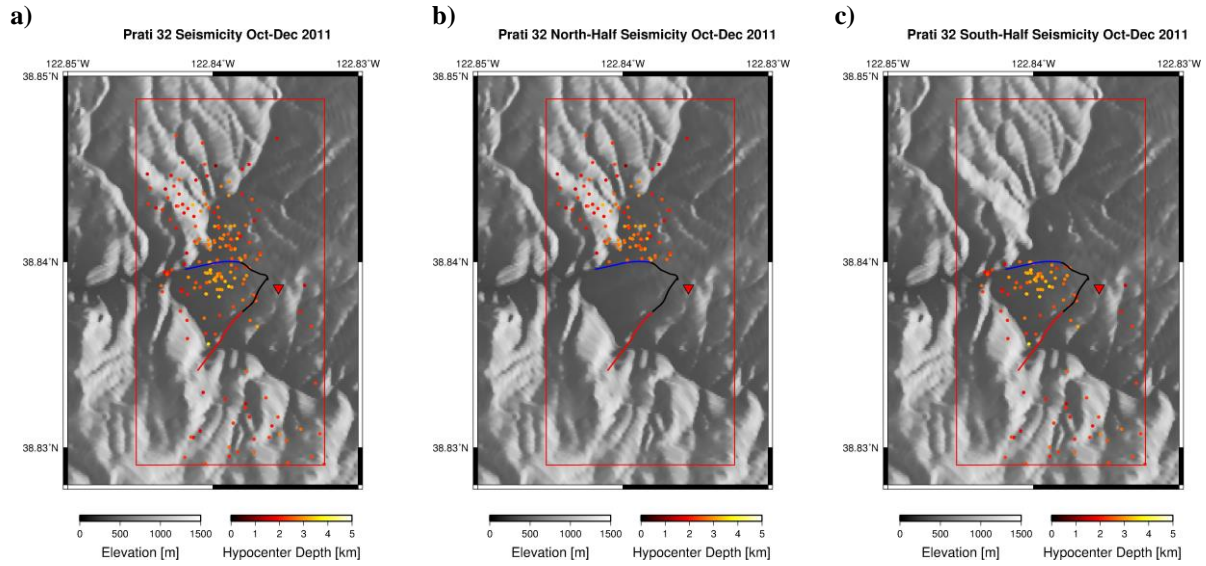
Figure 12: a) Map view of 192 earthquake locations recorded in the first three months of injection activities at Prati-32. b) Map view of a subset of 92 events located in the northern half of the study area. c) Map view of a subset of 100 events located in the southern half of the study area.

The results of the DDW analysis of the travel times associated with events in the northern half of the area are presented in Figure 13. The relatively small magnitudes (Mw=0.5-1.6) of these earthquakes resulted in a subset of 15 of the 34-station network to record these events, with a maximum station gap of 128°. A small station gap assures that the source region of the events is well sampled by the P- and S-wave rays, which is an important prerequisite for the assumptions made during WDD analysis (Lin and Shearer, 2007). Stations gaps of less than 150° are reasonable for WDD analysis. The conditions at The Geysers are well suited for this analysis, because the seismicity is shallow and occurs within the extent of the seismic network. The result of the L1-L2 norm fitting of the differential travel times based on waveform cross correlation is presented in Figure 13b. The linear fit yields a slope of 1.59 with a standard deviation of 0.04. This low Vp/Vs ratio is indicative of a gaseous fluid saturation likely indicating the presence of the previously mentioned steam plume in the highly fractured area to the north of Prati-32. The low Vp/Vs ratio is similar to Vp/Vs = 1.54 ± 0.05, which was reported by Gritto et al. (2016) for the Fumarole Area of The Geysers, where surface steam vents indicate the presence of gaseous fluids in the subsurface.
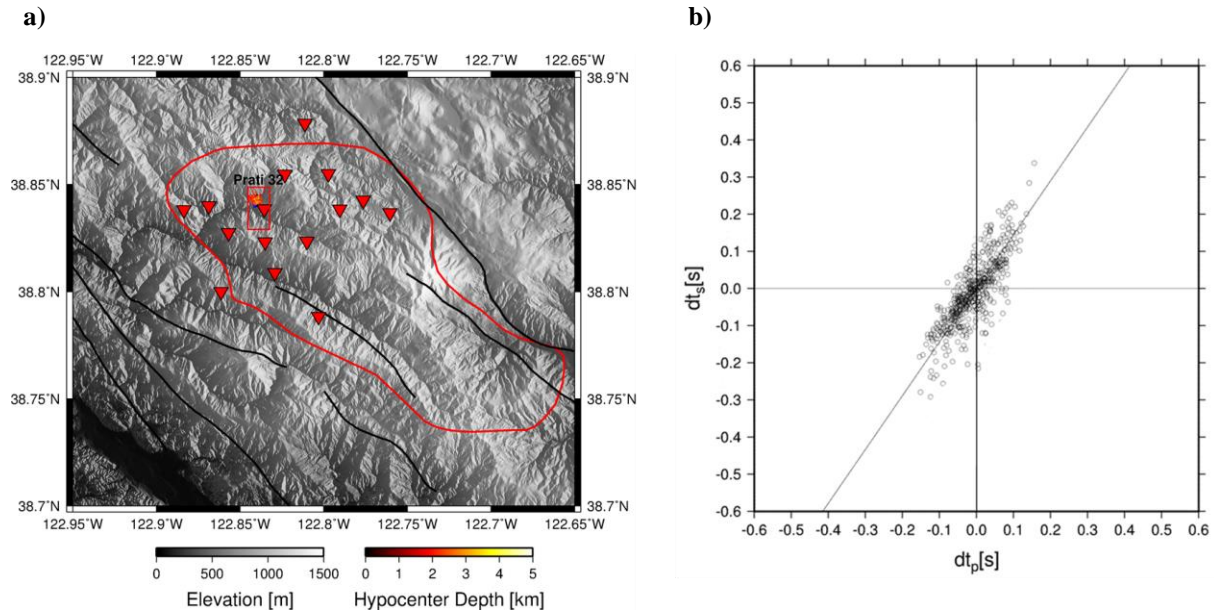

Figure 13: WDD analysis of earthquake data in the northern half of the Prati-32 study area (red rectangle). a) Map view of the seismic stations that recorded the seismicity in the northern half of the Prati-32 study area. Maximum station gap: 128°. b) Wadati diagram with P- and S-wave double difference travel times and linear fit based on the L1-L2 norm. Linear fit: 1.59 ± 0.04.

In contrast, the results for the southern half of the area are presented in Figure 14. Similar to the northern region, the low-magnitude seismicity (Mw 0.3-1.7) was recorded by 15 stations with a gap of 108º (Figure 14a). The results of the DDW analysis using L1-L2 norm fitting are presented in Figure 14b. The slope yielded a Vp/Vs ratio of 1.78 with a standard deviation of 0.03. This value is statistically insignificant from the pre-injection value (1.76 ± 0.04) for the total study region, which suggests that the area south of Prati-32 may not have experienced an increase in the volume of gaseous fluids. However, it is possible that the southern area contains liquid fluids that flash to steam during production. The Vp/Vs results suggest a steam concentration that is spatially correlated to the degree of fracturing below Prati-32.
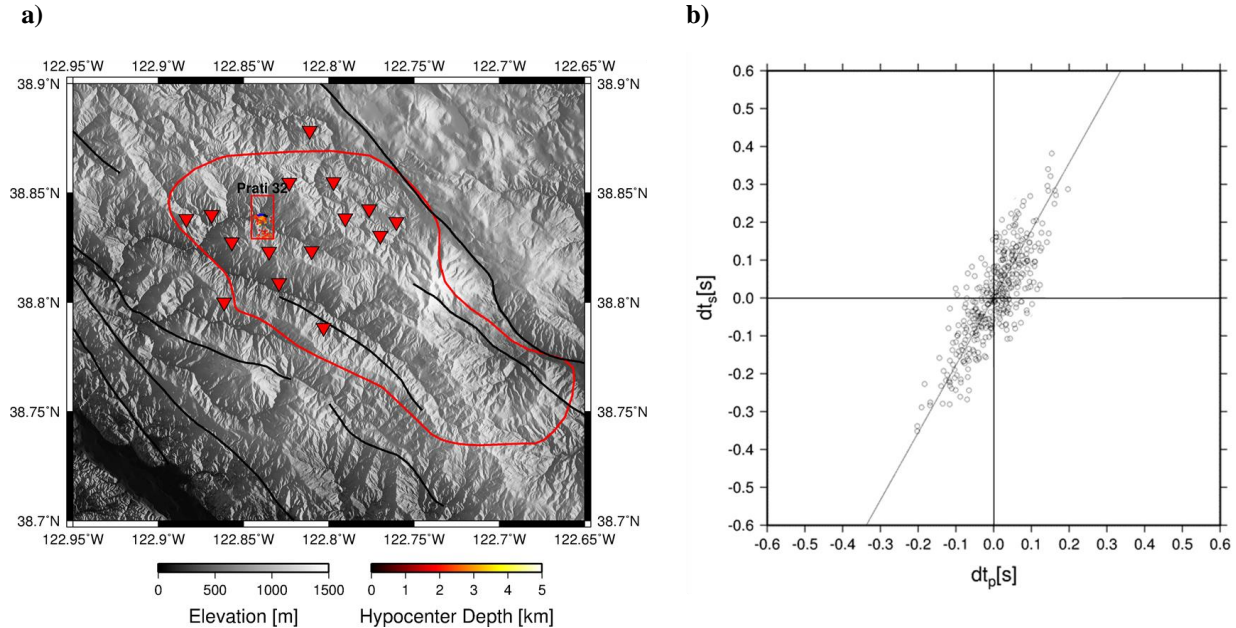
a)

b)

Figure 14: WDD analysis of earthquake data in the southern half of the Prati-32 study area (red rectangle). a) Map view of the seismic stations that recorded the seismicity in the southern half of the Prati-32 study area. Maximum station gap: 108º. b) Wadati diagram with P- and S-wave double difference travel times and linear fit based on the L1-L2 norm. Linear fit: 1.78 ± 0.03.

5. SUMMARY

During our project, we have developed technology to remotely estimate critical parameters for the characterization of the generated fracture network, which can support the geothermal industry during the development of EGS systems. We have investigated the seismicity associated with the water injection of The Geysers EGS Demonstration Project. The results show that there was a marked increase in the rate of seismicity in a 1x2 km region around the Prati-32 injection well as injection commenced on October 6, 2011. We have developed a semi-automated approach to estimate seismic moment tensors of the micro-earthquakes utilizing three-component seismic waveforms, which resulted in the compilation of a 166-event seismic moment tensor catalog for events ranging in moment magnitude from 0.7 to 3.9. The moment tensor catalog was subsequently utilized to invert for the stress tensor, and to investigate possible temporal changes resulting from the fluid injection. The results for inverting for the stress tensor demonstrate the quality of the seismic moment tensor catalog through the relatively small uncertainties in the recovered stress tensors. An approximate 15º counterclockwise rotation of σ_3 was found, accompanied by a rotation of σ_1 toward the vertical as the injected volume of water increased. The magnitude of these rotations is consistent with other nearby empirical observations (Martinez-Garzon et al., 2013) and thermo-hydromechanical simulation results (Jeanne et al., 2015) and indicate the evolution toward a more tensile stress state. We have estimated rupture area for earthquakes Mw 2.0 - 5.0 and found their scaling with moment magnitude to be consistent with published relationships developed for globally distributed earthquakes with larger magnitudes (Mw≥5.5). This scaling relationship in conjunction with results from the stress inversion was subsequently applied to a set of earthquakes with high location accuracy to generate a statistical representation of the 3D fracture network that was generated during the EGS demonstration project at Prati-32. We found that that the highest concentration of fractures is located approximately 300 m to the north and 400 m below the bottom of the injection and production wells. Given the uneven distribution of fractures in the study area, we applied the double-difference Wadati (DDW) technique to investigate spatial variations in the fluid saturations. Previous results by Gritto et al. (2016) had indicated that during the first three months of injection a steam plume developed in the study region below Prat-32. In the current study, it was shown that the steam plume is not symmetrically distributed within the 1x2 km study area, but appears to be more concentrated in the northern half of the study area.

Dreger et al.

REFERENCES

Dahm, T., and Fischer, T., (2013), "Velocity ratio variations in the source region of earthquake swarms in NW Bohemia obtained from arrival time double-differences." *Geoph.. J. Int.*, doi: 10.1093/gji/ggt410.

Dreger, D. S., (1997). The Large Aftershocks of the Northridge Earthquake and Their Relationship to Mainshock Slip and Fault-Zone Complexity, *Bull. Seism. Soc. Am.,* **87**, 1259-1266.

Dreger, D.S., Nadeau, R., and Chung, A., (2007), "Repeating Earthquake Finite-Source Models: Strong Asperities Revealed on the San Andreas Fault." *Geophys. Res. Lett.,* 34, L23302, doi:10.1029/2007GL031353.

Dreger, D.S., O.S. Boyd, R. Gritto, (2017), Estimating In-Situ Stress, Fracture Properties and Fluid Saturation During The Geysers EGS Demonstration Project, *Geothermal Resources Council Transactions*, Vol. 41, 2017, pp. 1-16.

Gritto, R. Dreger, D.S., Boyd, O.S., and Taira T. "Fluid Imaging, Moment Tensors and Finite Source Models During the EGS Demonstration Project at The Geysers, CA." *41st Workshop on Geothermal Reservoir Engineering*, February 22-24, 2016, Stanford University, Stanford, CA, (2016).

Gritto, R. and Jarpe, S.P., (2014), "Temporal variations of Vp/Vs-ratio at The Geysers geothermal field, USA." *Geothermics*, (2014), http://dx.doi.org/10.1016/j.geothermics.2014.01.012.

Gritto, R.; Daley, T. M.; Myer, L. R., (2004a), "Joint Cross Well and Single Well Seismic Studies of CO_2 Injection in an Oil Reservoir.", *Geophysical Prospecting*, 52, pp. 323-339.

Gritto, R.; Romero, A. E., Daley, T. M., (2004b), "Results of a VSP Experiment at the Resurgent Dome, Long Valley Caldera, California." *Geophys. Res. Lett.*, 31, No. 6, L06603, (2004b), 10.1029/2004GL019451.

Hardebeck, J. L., and Michael, A. J., (2004), "Stress orientations at intermediate angles to the San Andreas fault, California." *J. Geophys. Res.,* 109, no. B11303, doi: 10.1029/2004JB003239.

Hardebeck, J, and Michael, A., (2006), "Damped regional-scale stress inversions: Methodology and examples for southern California and the Coalinga aftershock sequence." *J. Geop. Res.*, doi:10.1029/2005JB004144.

Jeanne, P., Rutqvist, J., Dobson, P. F., Garcia, J., Walters, M., Hartline, C., and Borgia, A., (2015), "Geomechanical simulation of the stress tensor rotation caused by injection of cold water in a deep geothermal reservoir." *J. Geophys. Res.* 120, doi:10.1002/2015JB012414.

Julian B.R., Ross, A., Foulger, G.R., and Evans J.R., (1996), "Three-dimensional seismic image of a geothermal reservoir: The Geysers, California." *Geophys. Res. Lett.*, 23, (1996), doi:10.1029/96GL03321.

Leonard, M., (2000), Earthquake fault scaling: Self-consistent relating of rupture length, width, average displacement and moment release, Bull. Seism. Soc. Am., 100, no. 5a, 1971-1988.

Lin, G., and Shearer, P.M., "Estimating local Vp/Vs-ratios with similar earthquake 397 cluster." *Bull. Seism. Am.*, 97 (2), (2007), 379–388, http://dx.doi.org/10.1785/0120060115.

Lin, G., and Shearer, P.M. "Evidence for water-filled cracks in earthquake source regions." *Geophys. Res. Lett.*, 36, (2009), L17315, doi:10.1029/2009GL039098.

Lin, G. "Seismic investigation of magmatic unrest beneath Mammoth Mountain, California, USA." *Geology*, 41, (2013), 847-850, doi:10.1130/G34062.1.

Martinez-Garzon, P., Bohnhoff, M., Kwiatek, G., and Dresen, G. "Stress tensor changes related to fluid injection at The Geysers geothermal field, California." *Geophys. Res. Lett.*, 40, (2013), 2596-2601, doi: 10.1002/grl.50438.

Martinez-Garzon, P., Kwiatek, G., Ickrath, M., and Bohnhoff, M. "MSATSI: A MATLAB Package for Stress Inversion Combining Solid Classic Methodology, A New Simplified User-Handling, and a Visualization Tool." *Seism. Res. Lett.*, 85(4), (2014), 896-904, doi: 10.1785/0220130189.

Minson, S., and Dreger, D.S. "Stable Inversions for Complete Moment Tensors." *Geophys. Journ. Int.,* 174, (2008), 585-592.

Moos D., and Zoback, M. "In Situ Studies of Velocity in Fractured Crystalline Rocks." *J. Geophys. Res.*, 88, (1983), doi:10.1029/JB088iB03p02345.

Mori, J. (1993). Fault plane determinations for three small earthquakes along the San Jacinto Fault, California: Search for cross faults, *J. Geophys. Res.*, **98**, 17,711–17,722.

Mori, J. and S. Hartzell (1990). Source inversion of the 1988 Upland earthquake: determination of a fault plane for a small event, *Bull. Seism. Soc. Am.,* **80**, 507-518.

Pasyanos, M. E., Dreger, D. S., and Romanowicz B. (1996), "Towards Real-Time Determination of Regional Moment Tensors." *Bull. Seism. Soc. Am.*, 86, 1255-1269.

Vavrycuk, V. "Iterative joint inversion for stress and fault orientations from focal mechanisms.", (2014), *Geophys. J. Int.*, 199, 69-77, doi: 10.1093/gji/ggu224.

Wells, D. L., and K. L. Coppersmith, (1994). New empirical relationships among magnitude, rupture length, rupture width, rupture area and surface displacement, Bull. Seism. Soc. Am., 84, no. 4, 974-1002.